

Does Magnetic Field-Rotation Misalignment Solve the Magnetic Braking Catastrophe in Protostellar Disk Formation?

Zhi-Yun Li^{1,3}, Ruben Krasnopolsky^{2,3}, Hsien Shang^{2,3}

ABSTRACT

Stars form in dense cores of molecular clouds that are observed to be significantly magnetized. In the simplest case of a laminar (non-turbulent) core with the magnetic field aligned with the rotation axis, both analytic considerations and numerical simulations have shown that the formation of a large, 10^2 AU-scale, rotationally supported protostellar disk is suppressed by magnetic braking in the ideal MHD limit for a realistic level of core magnetization. This theoretical difficulty in forming protostellar disks is termed “magnetic braking catastrophe.” A possible resolution to this problem, proposed by Hennebelle & Ciardi and Joos et al., is that misalignment between the magnetic field and rotation axis may weaken the magnetic braking enough to enable disk formation. We evaluate this possibility quantitatively through numerical simulations. We confirm the basic result of Joos et al. that the misalignment is indeed conducive to disk formation. In relatively weakly magnetized cores with dimensionless mass-to-flux ratio $\gtrsim 5$, it enabled the formation of rotationally supported disks that would otherwise be suppressed if the magnetic field and rotation axis are aligned. For more strongly magnetized cores, disk formation remains suppressed, however, even for the maximum tilt angle of 90° . If dense cores are as strongly magnetized as indicated by OH Zeeman observations (with a mean dimensionless mass-to-flux ratio ~ 2), it would be difficult for the misalignment alone to enable disk formation in the majority of them. We conclude that, while beneficial to disk formation, especially for the relatively weak field case, the misalignment does not completely solve the problem of catastrophic magnetic braking in general.

Subject headings: accretion disks — ISM: magnetic fields — MHD — ISM: clouds

¹University of Virginia, Astronomy Department, Charlottesville, USA

²Academia Sinica, Institute of Astronomy and Astrophysics, Taipei, Taiwan

³Academia Sinica, Theoretical Institute for Advanced Research in Astrophysics, Taipei, Taiwan

1. Introduction

Star and planet formation are connected through disks. Disk formation, long thought to be a trivial consequence of angular momentum conservation during core collapse and star formation (e.g., Bodenheimer 1995), turned out to be much more complicated than originally envisioned. The complication comes from magnetic fields, which are observed in dense, star-forming, cores of molecular clouds (see Crutcher 2012 for a recent review). The field can strongly affect the angular momentum evolution of core collapse and disk formation through magnetic braking.

There have been a number of studies aiming at quantifying the effects of magnetic field on disk formation. In the ideal MHD limit, both analytic considerations and numerical simulations have shown that the formation of a rotationally supported disk (RSD hereafter) is suppressed by a realistic magnetic field (corresponding to a dimensionless mass-to-flux ratio of $\lambda \sim$ a few; Troland & Crutcher 2008) during the protostellar mass accretion phase in the simplest case of a non-turbulent core with the magnetic field aligned with the rotation axis (Allen et al. 2003; Galli et al. 2006; Price & Bate 2007; Mellon & Li 2008; Hennebelle & Fromang 2008; Dapp & Basu 2010; Seifried et al. 2011; Santos-Lima et al. 2012). The suppression of RSDs by excessive magnetic braking is termed “magnetic braking catastrophe” in star formation.

Rotationally supported disks are routinely observed, however, around evolved Class II young stellar objects (see Williams & Cieza 2011 for a review), and increasingly around Class I (e.g., Jørgensen et al. 2009; Lee 2011; Takakuwa et al. 2012) and even one Class 0 source (Tobin et al. 2012). When and how such disks form in view of the magnetic braking catastrophe is unclear. The current attempts to overcome the catastrophic braking fall into three categories: (1) non-ideal MHD effects, including ambipolar diffusion, Ohmic dissipation and Hall effect, (2) misalignment between magnetic and rotation axes, and (3) turbulence. Ambipolar diffusion does not appear to weaken the braking enough to enable large-scale RSD formation under realistic conditions (Krasnopolsky & Königl 2002; Mellon & Li 2009; Duffin & Pudritz 2009; Li et al. 2011). Ohmic dissipation can produce small, AU-scale, RSD in the early protostellar accretion phase (Machida et al. 2010; Dapp & Basu 2010; Dapp et al. 2012; Tomida et al. 2013). Larger, 10^2 AU-scale RSDs can be produced if the resistivity or the Hall coefficient of the dense core is much larger than the classical (microscopic) value (Krasnopolsky et al. 2010, 2011; see also Braiding & Wardle 2012a,b). Joos et al. (2012) explored the effects of tilting the magnetic field away from the rotation axis on disk formation (see also Machida et al. 2006; Price & Bate 2007; Hennebelle & Ciardi 2009). They concluded that Keplerian disks can form for a mass-to-flux ratio λ as low as 3, as long as the tilt angle is close to 90° (see their Fig. 14). The effects of turbulence were

explored by Santos-Lima et al. (2012, 2013), who concluded that a strong enough turbulence can induce enough magnetic diffusion to enable the formation of a 10^2 AU-scale RSD. Seifried et al. (2012) and Myers et al. (2012) considered supersonically turbulent massive cores. They found rotationally dominated disks around low-mass stars, although in both cases the turbulence-induced rotation is misaligned with the initial magnetic field by a large angle, which may have contributed to the disk formation (see also Joos et al. 2013).

The goal of this paper is to revisit the role of magnetic field-rotation misalignment in disk formation. The misalignment is expected if the angular momenta of dense cores are generated through turbulent motions (e.g., Burkert & Bodenheimer 2000; Myers et al. 2012). It is also inferred from the misalignment between the field direction traced by polarized dust emission and the outflow axis, which is taken as a proxy for the direction of rotation (Hull et al. 2012). Indeed, in the CARMA sample of Hull et al., the distribution of the angle θ_0 between the magnetic field and jet/rotation axis is consistent with being random. If true, it would indicate that in half of the sources the two axes are misaligned by a large angle of $\theta_0 > 60^\circ$ (see however Chapman et al. 2013 and discussion in §5.2). Such a large misalignment would be enough to allow disk formation in dense cores magnetized to a realistic level (with λ of a few; Troland & Crutcher 2008) according to Joos et al. (2012). If the alignment angle θ_0 is indeed random and Joos et al.’s conclusions are generally true, the magnetic braking catastrophe would be largely solved. Given their far-reaching implications, it is prudent to check Joos et al.’s conclusions, using a different numerical code. It is the task of this paper.

We carry out numerical experiments of disk formation in dense cores with misaligned magnetic and rotation axes using non-ideal MHD code Zeus-TW that includes self-gravity. We find that a large misalignment angle does indeed enable the formation of RSDs in weakly magnetized dense cores with dimensionless mass-to-flux ratios $\gtrsim 5$, but not in dense cores magnetized to higher, more typical levels. Our conclusion is that while the misalignment helps with disk formation, especially in relatively weakly magnetized cores, it may not provide a complete resolution to the magnetic braking catastrophe by itself.

The rest of the paper is organized as follows. In §2, we describe the model setup. The numerical results are described in §3 and §4. We compare our results to those of Joos et al. and discuss their implications in §5 and conclude with a short summary in §5.3.

2. Problem Setup

We follow Li et al. (2011) and Krasnopolsky et al. (2012) and start our simulations from a uniform, spherical core of $1 M_\odot$ and radius 10^{17} cm in a spherical coordinate system

(r, θ, ϕ) . The initial density $\rho_0 = 4.77 \times 10^{-19} \text{ g cm}^{-3}$ corresponds to a molecular hydrogen number density of 10^5 cm^{-3} . We adopt an isothermal equation of state with a sound speed $a = 0.2 \text{ km s}^{-1}$ below a critical density $\rho_c = 10^{-13} \text{ g cm}^{-3}$, and a polytropic equation of state $p \propto \rho^{5/3}$ above it. At the beginning of the simulation, we impose a solid-body rotation of angular speed $\Omega_0 = 10^{-13} \text{ s}^{-1}$ on the core, with axis along the north pole ($\theta = 0$). It corresponds to a ratio of rotational to gravitational binding energy of 0.025, which is typical of the values inferred for NH_3 cores (Goodman et al. 1993). The initial magnetic field is uniform, tilting away from the rotation axis by an angle θ_0 . We consider three values for the initial field: $B_0 = 10.6, 21.3$ and $35.4 \mu\text{G}$, corresponding to dimensionless mass-to-flux ratio, in units of $(2\pi G^{1/2})^{-1}$, $\lambda = 9.72, 4.86$ and 2.92 , respectively, for the core as a whole. The mass-to-flux ratio for the central flux tube λ_c is higher than the global value λ by 50%, so that $\lambda_c = 14.6, 7.29$ and 4.38 for the three cases respectively. The effective mass-to-flux ratio λ_{eff} should lie between these two limits. If the star formation efficiency per core is $\sim 1/3$ (e.g., Alves et al. 2007), then one way to estimate λ_{eff} is to consider the (cylindrical) magnetic flux surface that encloses $1/3$ of the core mass, which yields $\lambda_{\text{eff}} = 1.41\lambda$, corresponding to 13.7, 6.85, and 4.12 for the three cases respectively; the fraction $1/3$ is also not far from the typical fraction of core mass that has accreted onto the central object at the end of our simulations (see Table 1). For the tilt angle, we also consider three values: $\theta_0 = 0^\circ, 45^\circ$ and 90° . The $\theta_0 = 0^\circ$ corresponds to the aligned case, with the magnetic field and rotation axis both along the z -axis ($\theta = 0$). The $\theta_0 = 90^\circ$ corresponds to the orthogonal case, with the magnetic field along the x -axis ($\theta = 90^\circ, \phi = 0$). Models with these nine combinations of parameters are listed in Table 1; additional models are discussed below.

As in Krasnopolsky et al. (2012), we choose a non-uniform grid of $96 \times 64 \times 60$. In the radial direction, the inner and outer boundaries are located at $r = 10^{14}$ and 10^{17} cm, respectively. The radial cell size is smallest near the inner boundary (5×10^{12} cm or ~ 0.3 AU). It increases outward by a constant factor ~ 1.08 between adjacent cells. In the polar direction, we choose a relatively large cell size (7.5°) near the polar axes, to prevent the azimuthal cell size from becoming prohibitively small; it decreases smoothly to a minimum of $\sim 0.63^\circ$ near the equator, where rotationally supported disks may form. The grid is uniform in the azimuthal direction.

The boundary conditions in the azimuthal direction are periodic. In the radial direction, we impose the standard outflow boundary conditions. Material leaving the inner radial boundary is collected as a point mass (protostar) at the center. It acts on the matter in the computational domain through gravity. On the polar axes, the boundary condition is chosen to be reflective. Although this is not strictly valid, we expect its effect to be limited to a small region near the axis.

Table 1. Models

Model	λ^a	λ_{eff}^b	θ_0	η ($10^{17} \text{ cm}^2 \text{ s}^{-1}$)	M_*^c (M_\odot)	RSD ^d
A	9.72	13.7	0°	1	0.24	No
B	4.86	6.85	0°	1	0.22	No
C	2.92	4.12	0°	1	0.33	No
D	9.72	13.7	45°	1	0.21	Yes/Porous
E	4.86	6.85	45°	1	0.35	No
F	2.92	4.12	45°	1	0.27	No
G	9.72	13.7	90°	1	0.38	Yes/Robust
H	4.86	6.85	90°	1	0.46	Yes/Porous
I	2.92	4.12	90°	1	0.47	No
M	9.72	13.7	90°	0	0.10	Yes/Robust
N	9.72	13.7	90°	0.1	0.26	Yes/Robust
P	4.03	5.68	90°	1	0.25	Yes/Porous
Q	3.44	4.85	90°	1	0.14	No

Note. — a). The average dimensionless mass-to-flux ratio for the core as a whole; b). The effective mass-to-flux ratio for the central 1/3 of the core mass (see §2 for discussion); c). Mass of the central object when the simulation is stopped; d). “Robust” disks are persistent, rotationally supported structures that rarely display large deviations from smooth Keplerian motions, whereas “porous” disks are highly active, rotationally dominated structures with large distortions and may occasionally be completely disrupted.

We initially intended to carry out simulations in the ideal MHD limit, so that they can be compared more directly with other work, especially Joos et al. (2012). However, ideal MHD simulations tend to produce numerical “hot zones” that force the calculation to stop early in the protostellar mass accretion phase, a tendency we noted in our previous 2D (Mellon & Li 2008) and 3D simulations (Krasnopolsky et al. 2012). To lengthen the simulation, we include a small, spatially uniform resistivity $\eta = 10^{17} \text{ cm}^2 \text{ s}^{-1}$. We have verified that, in the particular case Model G ($\lambda = 9.72$ and $\theta_0 = 90^\circ$), this resistivity changes the flow structure little compared to either the ideal MHD Model M (before the latter stops) or Model N, where the resistivity is reduced by a factor 10, to $10^{16} \text{ cm}^2 \text{ s}^{-1}$.

3. Weak-Field Case: Disk Formation Enabled by Field-Rotation Misalignment

3.1. Equatorial Pseudodisk vs Magnetically Induced Curtain

To illustrate the effect of the misalignment between the magnetic field direction and rotation axis, we first consider an extreme case where the magnetic field is rather weak (with a mass-to-flux ratio $\lambda = 9.72$ for the core as a whole and $\lambda_{\text{eff}} = 13.7$ for the inner 1/3 of the core mass). In this case, a well-formed rotationally supported disk is present in the orthogonal case with $\theta_0 = 90^\circ$ (Model G in Table 1). Such a disk is absent in the aligned case (with $\theta_0 = 0^\circ$, Model A). The contrast is illustrated in Fig. 1, where we plot snapshots of the aligned and orthogonal cases at a representative time $t = 3.9 \times 10^{12} \text{ s}$, when a central mass of 0.11 and 0.12 M_\odot , respectively, has formed. The flow structures in the two cases are very different in both the equatorial (panels [a] and [b]) and meridian (panels [c] and [d]) plane. In the equatorial plane, the aligned case has a relatively large (with radius $\sim 10^{16} \text{ cm}$) over-dense region where material spirals rapidly inward. On the (smaller) scale of 10^{15} cm , the structure is dominated by expanding, low-density lobes; they are the decoupling enabled magnetic structures (DEMS for short) that have been studied in detail by Zhao et al. (2011) and Krasnopolsky et al. (2012). No rotationally supported disk is evident. The equatorial structure on the 10^{16} cm scale in the orthogonal case is dominated by a pair of spirals instead. The spirals merge, on the 10^{15} cm scale, into a more or less continuous, rapidly rotating structure — a rotationally supported disk. Clearly, the accretion flow in the orthogonal case was able to retain more angular momentum than in the aligned case. Why is this the case?

A clue comes from the meridian view of the two cases (panels [c] and [d] of Fig. 1). In the aligned case, there is a strong bipolar outflow extending beyond $3 \times 10^{16} \text{ cm}$ at the relatively early time shown. The outflow forces most of the infalling material to accrete through a flattened equatorial structure — an over-dense pseudodisk (Galli & Shu 1993; see

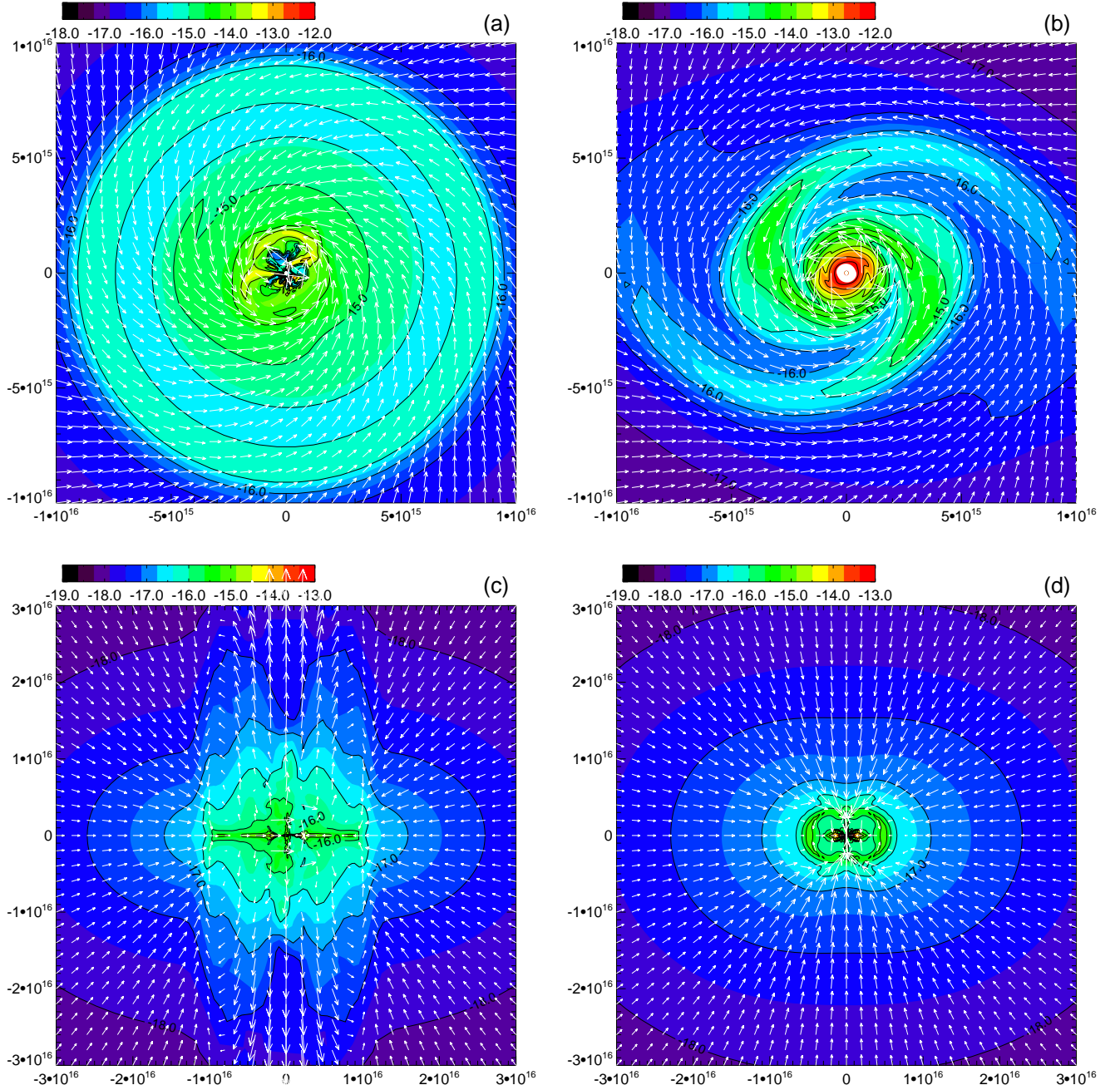


Fig. 1.— Snapshots of the logarithm of density (color map, in units of g cm^{-3}) and velocity field (white arrows) for the weakly magnetized core of $\lambda = 9.72$ at a representative time $t = 3.9 \times 10^{12}$ s. The left (right) panels are for the aligned (orthogonal) case, and the top (bottom) panels are for the equatorial $x-y$ (meridian $y-z$) plane. Note the powerful bipolar outflow in panel (c) driven by the pseudodisk in panel (a). The lack of powerful outflow in panel (d) is indicative of a weaker magnetic braking, which is consistent with the presence of a rotationally supported disk in panel (b). The length unit is cm. The scale in (c) and (d) is three times larger than that in (a) and (b).

panel [a] for a face-on view of the pseudodisk, noting the difference in scale between panel [c] and [a]). It is the winding of the magnetic field lines by the rotating material in the pseudodisk that drives the bipolar outflow in the first place. The wound-up field lines act back on the pseudodisk material, braking its rotation. It is the efficient magnetic braking in the pseudodisk that makes it difficult for rotationally supported disks to form in the aligned case.

The prominent bipolar outflow indicative of efficient magnetic braking is absent in the orthogonal case, as was emphasized by Ciardi & Hennebelle (2010). It is replaced by a much smaller, shell-like structure inside which the 10^{15} cm-scale rotationally supported disk is encased (panel [d]). To understand this difference in flow structure pictorially, we plot in Fig. 2 the three-dimensional structure of the magnetic field lines on the scale of 1000 AU (or 1.5×10^{16} cm), which is 50% larger than the size of panels (a) and (b) of Fig. 1, but half of that of panels (c) and (d). Clearly, in the aligned case, the relatively weak initial magnetic field (corresponding to $\lambda \approx 10$) has been wound up many turns by the material in the equatorial pseudodisk, building up a magnetic pressure in the equatorial region that is released along the polar directions (see the first panel of Fig. 2). The magnetic pressure gradient drives a bipolar outflow, which is evident in panel (c) and in many previous simulations of magnetized core collapse, including the early ones such as Tomisaka (1998) and Allen et al. (2003). In contrast, in the orthogonal case, the equatorial region is no longer the region of the magnetically induced pseudodisk. In the absence of rotation (along the z -axis), the dense core material would preferentially contract along the field lines (that are initially along the x -axis) to form a dense sheet in the y - z plane that passes through the origin. The twisting of this sheet by rotation along the z -axis produces two curved “curtains” that spiral smoothly into the disk at small distances, somewhat analogous in shape to two snail-shells (see the second panel of Fig. 2).

The snail-shaped dense curtain in the orthogonal case naturally explains the morphology of the density maps shown in panels (b) and (d) of Fig. 1. First, the two prominent spiral arms in the panel (a) are simply the equatorial (x - y) cut of the curved curtains. An interesting feature of the spirals (and the snail-shaped dense curtain as a whole) is that they are the region where the magnetic field lines change directions sharply. This is illustrated in Fig. 3, which is similar to panel (b) of Fig. 1, except that the magnetic vectors (rather than velocity vectors) are plotted on top of the density map. Clearly, the spirals separate the field lines rotating counter clock-wise (lower-right part of the figure) from those rotating close-wise (upper-left). The sharp kink is analogous to the well-known field line kink across the equatorial pseudodisk in the aligned case, where the radial component of the magnetic field changes direction. It supports our interpretation of the spirals and, by extension, the curtain as a magnetically induced feature, as is the case of pseudodisk. In other words, the

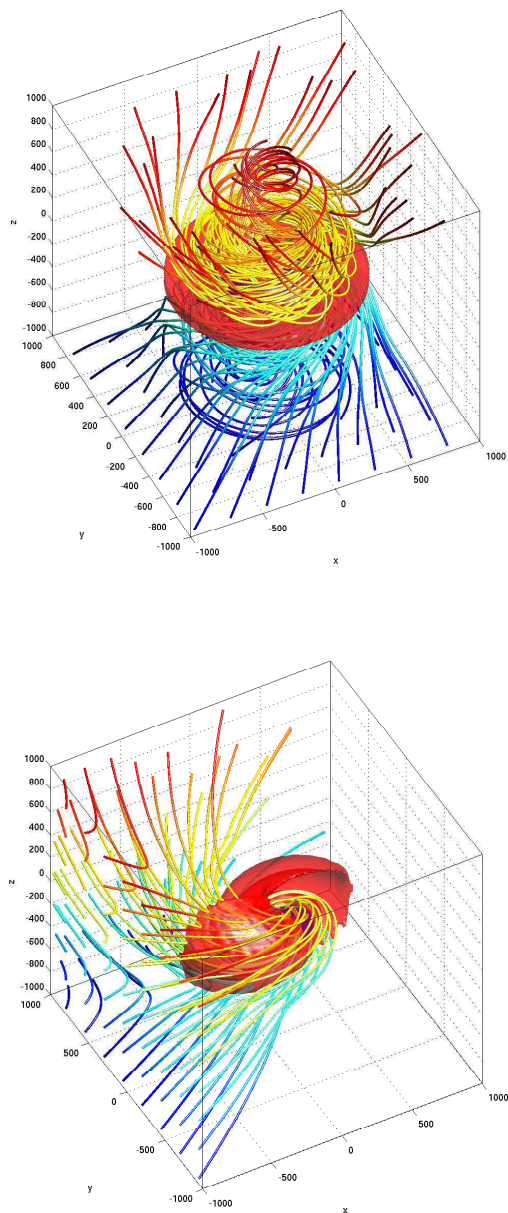


Fig. 2.— 3D view of representative magnetic field lines and isodensity surfaces at $\rho = 10^{-16}$ (red) and 10^{-15} g cm $^{-3}$ (blue) for the aligned Model A and orthogonal Model G. For clarity, only field lines originated from the bottom x - y and left y - z plane are plotted, respectively. Note that the magnetically induced equatorial pseudodisk in the aligned case is warped by rotation into two snail-shaped curtains that spiral inward to form a disk (blue surface) in the orthogonal case. The length is in units of AU.

spirals are not produced by gravitational instability in a rotationally supported structure; they are “pseudospirals” in the same sense as the “pseudodisks” of Galli & Shu (1993). The field line kinks are also evident across the dense curtain in the 3D structure shown in the second panel of Fig. 2.

The 3D topology of the magnetic field and the dense structures that it induces lie at the heart of the difference in the magnetic braking efficiency between the aligned and orthogonal case. In particular, a flattened, rotating, equatorial pseudodisk threaded by an ordered magnetic field with an appreciable vertical component (along the rotation axis) is more conducive to driving an outflow than a warped curtain with a magnetic field predominantly tangential to its surface. The outflow plays a key role in angular momentum removal and the suppression of rotationally supported disks, as we demonstrate next.

3.2. Torque Analysis

To quantify the outflow effect, we follow Zhao & Li (2013; see also Joos et al. 2012) and compare the rates of angular momentum change inside a finite volume V through its surface S due to infall and outflow to that due to magnetic torque. The total magnetic torque relative to the origin (from which a radius vector \mathbf{r} is defined) is

$$\mathbf{N}_m = \frac{1}{4\pi} \int [\mathbf{r} \times ((\nabla \times \mathbf{B}) \times \mathbf{B})] dV, \quad (1)$$

where the integration is over the volume V . Typically, the magnetic torque comes mainly from the magnetic tension rather than pressure force. The dominant magnetic tension term can be simplified to a surface integral (Matsumoto & Tomisaka 2004)

$$\mathbf{N}_t = \frac{1}{4\pi} \int (\mathbf{r} \times \mathbf{B})(\mathbf{B} \cdot d\mathbf{S}), \quad (2)$$

over the surface S of the volume. This volume-integrated magnetic torque is to be compared with the rate of angular momentum advected into the volume through fluid motion,

$$\mathbf{N}_a = - \int \rho(\mathbf{r} \times \mathbf{v})(\mathbf{v} \cdot d\mathbf{S}), \quad (3)$$

which will be referred to as the advective torque below.

Since the initial angular momentum of the dense core is along the z -axis, we will be mainly concerned with the z -component of the magnetic and advective torque which, for a spherical volume inside radius r , are given by

$$N_{t,z} = \frac{1}{4\pi} \int \varpi B_\phi B_r dS, \quad (4)$$

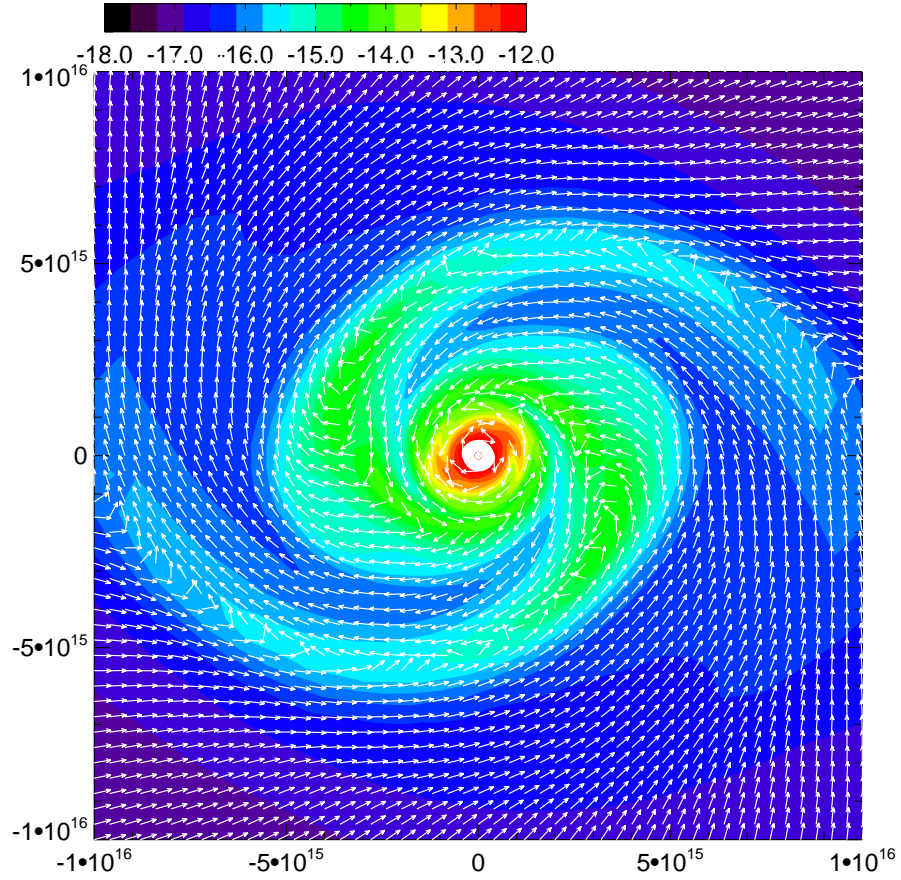


Fig. 3.— Same as panel (b) of Fig. 1 but with magnetic unit vectors instead of velocity vectors plotted. Note that the field lines kink sharply in the spirals. The kinks demonstrate that the spirals (and the curtain that contains them) are the counterparts to the equatorial pseudodisk in the aligned case.

and

$$N_{a,z} = - \int \rho \varpi v_\phi v_r dS. \quad (5)$$

The advective torque consists of two parts: the rates of angular momentum advected into and out of the sphere by infall and outflow respectively:

$$N_{a,z}^{\text{in}} = - \int \rho \varpi v_\phi v_r (< 0) dS, \quad (6)$$

and

$$N_{a,z}^{\text{out}} = - \int \rho \varpi v_\phi v_r (> 0) dS. \quad (7)$$

An example of the magnetic and advective torques is shown in Fig. 4. The torques are evaluated on spherical surfaces of different radii, at the representative time $t = 3.9 \times 10^{12}$ s. For the aligned case, the net torque close to the central object is nearly zero up to a radius of $\sim 2 \times 10^{15}$ cm, indicating that the angular momentum advected inward is nearly completely removed by magnetic braking there. At larger distances, between $\sim 2 \times 10^{15}$ and $\sim 10^{16}$ cm, the net torque $N_{t,z} + N_{a,z}$ is negative, indicating that the angular momentum of the material inside a sphere of radius in this range decreases with time. This is in sharp contrast with the orthogonal case, where the net torque is positive in that radial range, with the angular momentum there increasing (rather than decreasing) with time. One may think that the difference is mainly due to a significantly larger magnetic torque $N_{t,z}$ in the aligned case than in the orthogonal case. Although this is typically the case at early times, the magnetic torques in the two cases become comparable at later times (see the lowest solid lines in the two panels of Fig. 4; a movie of the torques is available on request from the authors). A bigger difference comes from the total (or net) angular momentum $N_{a,z} = N_{a,z}^{\text{in}} + N_{a,z}^{\text{out}}$ advected inward, which is substantially smaller in the aligned case than in the orthogonal case (see the uppermost solid lines in the two panels). The main reason for the difference is that a good fraction of the angular momentum advected inward by infall $N_{a,z}^{\text{in}}$ is advected back out by outflow $N_{a,z}^{\text{out}}$ in the former, but not the latter. This is helped by the fact that $N_{a,z}^{\text{in}}$ is somewhat smaller in the aligned case to begin with (compare the dotted lines in the two panels). The lack of appreciable outward advection of angular momentum by outflow, which is itself a product of field-winding and magnetic braking in the aligned case, appears to be the main reason for the orthogonal case to retain more angular momentum at small radii and form a rotationally supported disk in this particular case of relatively weak magnetic field.

The formation of a rotationally supported disk can be seen most clearly in Fig. 5, where we plot the infall and rotation speed, as well as specific angular momentum as a function of radius along 4 ($\pm x$ and $\pm y$) directions in the equatorial plane. In the orthogonal case, the

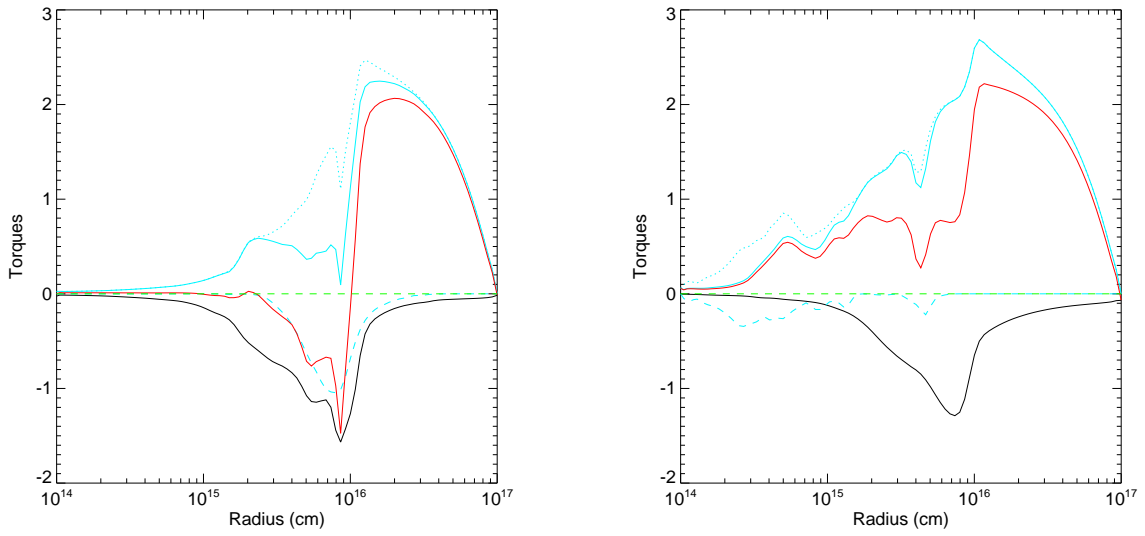


Fig. 4.— Magnetic (black solid line, $N_{t,z}$) and total advective (magenta, $N_{a,z}$) torque acting on spheres of different radii for the aligned (left panel) and orthogonal (right) case at the representative time $t = 3.9 \times 10^{12}$ s. Also plotted are the net torque (red, $N_{t,z} + N_{a,z}$), and the contributions to the advective torque by infall (dotted, $N_{a,z}^{\text{in}}$) and outflow (dashed, $N_{a,z}^{\text{out}}$). Note that the net torque is negative between $\sim 2 \times 10^{15}$ and $\sim 10^{16}$ cm for the aligned case but positive for the orthogonal case, mainly because the outflow removes more angular momentum in the former than in the latter.

infall and rotation speeds display the two tell-tale signs of rotationally supported disks: (1) a slow, subsonic (although nonzero) infall speed much smaller than the free fall value, and (2) a much faster rotation speed close to the Keplerian value inside a radius of ~ 100 AU. The absence of a rotationally supported disk in the aligned case is just as obvious. It has a rotation speed well below the Keplerian value and an infall speed close to the free fall value, especially at small radii up to ~ 100 AU. This corresponds to the region dominated by the low-density, strongly magnetized, expanding lobes (i.e., DEMS; see panel [a] of Fig 1) where the angular momentum is almost completely removed by a combination of magnetic torque and outflow (see the third panel in Fig. 5). Also evident from the panel is that the specific angular momentum of the equatorial inflow drops significantly twice: near $\sim 10^{15}$ and $\sim 10^{16}$ cm respectively. The former corresponds to the DEMS-dominated region, and the latter the pseudodisk (see panel [a] of Fig. 1). The relatively slow infall inside the pseudodisk allows more time for magnetic braking to remove angular momentum. It is the pseudodisk (and its associated outflow) working in tandem with the DEMS that suppresses the formation of a rotationally supported disk in the aligned case. Interestingly, there is a bump near $\sim 10^{16}$ cm for the specific angular momentum of the orthogonal case, indicating that the angular momentum in the equatorial plane is transported radially outward along the spiraling field lines from small to large distances (see Fig. 3).

The spiraling equatorial field lines in the orthogonal Model G have an interesting property: they consist of two strains of opposite polarity. As the strains get wound up more and more tightly by rotation at smaller and smaller radii, field lines of opposite polarity are pressed closer and closer together, creating a situation that is conducive to reconnection, either of physical or numerical origin (see the first panel of Fig. 6). Model G contains a small but finite resistivity ($\eta = 10^{17} \text{ cm}^2 \text{ s}^{-1}$). It does not appear to be responsible for the formation and survival of the Keplerian disk, because a similar disk is also formed at the same (relatively early) time for a smaller resistivity of $\eta = 10^{16} \text{ cm}^2 \text{ s}^{-1}$ (Model N) and even without any explicit resistivity (Model M). Numerical resistivity may have played a role here, but it is difficult to quantify at the moment. In any case, the magnetic field on the Keplerian disk appears to be rather weak, as can be seen from the second panel of Fig. 6, where the plasma β is plotted along 4 ($\pm x$ and $\pm y$) directions in the equatorial plane. On the Keplerian disk in the orthogonal Model G (inside ~ 100 AU), β is of order 10^2 or more, indicating that there is more matter accumulating in the disk than magnetic field, either because the matter slides along the field lines into the disk (increasing density but not the field strength) or because of numerical reconnection that weakens the field, or both. This situation is drastically different from the aligned case, where the inner 100 AU region is heavily influenced by the magnetically-dominated low-density lobes.

4. Moderately Strong Field Cases: Difficulty with Disk Formation

We have seen from the preceding section that, in the weakly magnetized case of $\lambda = 9.72$, the 10^2 AU-scale inner part of the protostellar accretion flow is dominated by two very different types of structures: a weakly magnetized, dense, rotationally supported disk (RSD) in the orthogonal case ($\theta_0 = 90^\circ$, Model G) and magnetically dominated, low-density lobes or DEMS in the aligned case ($\theta_0 = 0^\circ$, Model A), at least at the relatively early time discussed in §3, when the central mass reaches $\sim 0.1 M_\odot$. This dichotomy persists to later times for these two models and for other models as well, as illustrated by Fig. 7, where we plot Models A–I at a time when the central mass reaches $0.2 M_\odot$. It is clear that the RSD for Model G becomes even more prominent at the later time, although a small magnetically dominated, low-density lobe is evident close to the center of the disk: it is a trapped DEMS that is too weak to disrupt the disk. In this case, the identification of a robust RSD is secure, at even later times (up to the end of the simulation, when the central mass reaches $0.38 M_\odot$ or 38% of the initial core mass). In the aligned case (Model A), the inner accretion flow remains dominated by the highly dynamic DEMS at late times, with no sign of RSD formation.

For the intermediate tilt angle case of $\theta_0 = 45^\circ$ (Model D), the inner structure of the protostellar accretion flow is shaped by the tussle between RSD and DEMS. Fig. 7 shows that, at the plotted time, Model D has several spiral arms that appear to merge into a rotating disk. There are, however, at least three low-density “holes” near the center of the disk: they are the magnetically dominated DEMS. Movies show that the highly variable DEMS are generally confined close to the center, although they can occasionally expand to occupy a large fraction of the disk surface. Overall, the circumstellar structure in Model D is more disk-like than DEMS-like. We shall call it a “porous disk,” to distinguish it from the more filled-in, more robust disk in the orthogonal Model G. Even though most of the porous disk has a rotation speed dominating the infall speed, the infall is highly variable, and often supersonic. The rotation speed also often deviates greatly from the Keplerian value. Such an erratic disk is much more dynamic than the quiescent disks envisioned around relatively mature (e.g., Class II) YSOs. The intermediate tilt angle case drives a powerful bipolar outflow, unlike the orthogonal case, but similar to the aligned case. This is consistent with the rate of angular momentum removal increasing with decreasing tilt angle (i.e., from 90° to 45° ; see also Ciardi & Hennebelle 2010).

As the strength of the initial magnetic field in the core increases, the DEMS becomes more dominant. This is illustrated in the middle column of Fig. 7, where the three cases with an intermediate field strength corresponding to $\lambda = 4.86$ (and $\lambda_{\text{eff}} = 6.85$) are plotted. In Model H, where the magnetic and rotation axes are orthogonal, a relatively small (with radius of $\sim 10^2$ AU) rotationally dominated disk is clearly present at the time shown. As in

the weaker field case of Model G, it is fed by prominent “pseudo-spirals” which are part of a magnetically-induced curtain in 3D (see the second panel of Fig. 2). Compared to Model G, the curtain here is curved to a lesser degree, which is not surprising because the rotation is slower due to a more efficient braking and the stronger magnetic field embedded in the curtain is harder to bend. The disk is also smaller, less dense, and more dynamic. It is more affected by DEMS, which occasionally disrupt the disk, although it always reforms after disruption. Overall, the circumstellar structure in Model H is more RSD-like than DEMS-like. As in Model D, we classify it as a “porous disk.” As the tilt angle decreases from 90° to 45° (Model E) and further to 0° (Model B), the rotationally dominated circumstellar structure largely disappears; it is replaced by DEMS-dominated structures. Even though there is still a significant amount of rotation in the accretion flow, a dense coherent disk is absent. We conclude that for a moderately strong magnetic field of $\lambda = 4.86$ the formation of RSD is suppressed if the tilt angle is moderate.

In the cases of the strongest magnetic field corresponding to $\lambda = 2.92$ (and $\lambda_{\text{eff}} = 4.12$), the formation of RSD is suppressed regardless of the tilt angle, as can be seen from the last column of Fig. 7. For the orthogonal case (Model I), the prominent “pseudo-spirals” in the weaker field cases of Model G ($\lambda = 9.72$) and H ($\lambda = 4.86$) are replaced by two arms that are only slightly bent. They are part of a well-defined pseudodisk that happens to lie roughly in the $y = 0$ (or $x-z$) plane (see the second panel of Fig. 8). In the absence of any initial rotation, one would expect the pseudodisk to form perpendicular to the initial field direction along the x -axis, i.e., in the $x = 0$ (or $y-z$) plane. Over the entire course of core evolution and collapse, the rotation has rotated the expected plane of the pseudodisk by nearly 90° . Nevertheless, at the time shown (when the central mass reaches $0.2 M_\odot$), there is apparently little rotation left inside 10^3 AU to warp the pseudodisk significantly. Except for the orientation, this pseudodisk looks remarkably similar to the familiar one in the aligned case (Model C; see the first panel of Fig. 8). In particular, there are low-density “holes” in the inner part of both pseudodisks which are threaded by intense magnetic fields and surrounded by dense filaments: they are the DEMS. In the intermediate tilt angle case of 45° (Model F, not shown in the 3D figure), the pseudodisk is somewhat more warped than the two other cases, and its inner part is again dominated by DEMS. It is clear that for a magnetic field of λ of a few, the inner circumstellar structure is dominated by the magnetic field, with rotation playing a relatively minor role; the RSD remains suppressed despite the misalignment.

To better estimate the boundary between the cores that produce RSDs and those that do not, we carried out two additional simulations with $\theta_0 = 90^\circ$ (Models P and Q in Table 1). We found a porous disk in Model P ($\lambda = 4.03$ and $\lambda_{\text{eff}} = 5.68$), as in the weaker field case of Model H, but no disk in Model Q ($\lambda = 3.44$ and $\lambda_{\text{eff}} = 4.85$), as in the stronger field case of

Model I. From this, we infer that the boundary lies approximately at $\lambda \approx 3.5$ (or $\lambda_{\text{eff}} \approx 5$).

5. Discussion

5.1. Comparison with Joos et al.

Our most important qualitative result is that the misalignment between the magnetic field and rotation axis tends to promote the formation of rotationally supported disks, especially in weakly magnetized dense cores. This is in agreement with the conclusion previously reached by Joos et al. (2012; JHC12 hereafter), using a different numerical code and somewhat different problem setup. Their calculations were carried out using an adaptive mesh refinement (AMR) code in the Cartesian coordinate system, with the central object treated using a stiffening of the equation of state, whereas ours were done using a fixed mesh refinement (FMR) code in the spherical coordinate system, with an effective sink particle at the origin. Despite the differences, these two distinct sets of calculations yield qualitatively similar results. The case for the misalignment promoting disk formation is therefore strengthened.

Quantitatively, there appears to be a significant discrepancy between our results and theirs. According to their Fig. 14, a Keplerian disk is formed in the relatively strongly magnetized case of $\lambda = 3$ if the misalignment angle $\theta_0 = 90^\circ$. Formally, this case corresponds roughly to our Model I ($\lambda = 2.92$ and $\theta_0 = 90^\circ$), for which we can rule out the formation of a rotationally supported disk with confidence (see Fig. 7).

We believe that the discrepancy comes mostly from the initial density profile adopted, which affects the degree of magnetization near the core center for a given global mass-to-flux ratio λ . Joos et al. adopted a centrally condensed initial mass distribution

$$\rho(r) = \frac{\rho_0}{1 + (r/r_0)^2} \quad (8)$$

with the characteristic radius r_0 set to $1/3$ of the core radius R_c , so that the central-to-edge density contrast is 10 (see also Ciardi & Hennebelle 2010). It is easy to show that, for this density profile and a uniform magnetic field, the mass-to-flux ratio for the flux tube passing through the origin is

$$\lambda_c = \frac{x_0^2 \arctan x_0}{2(x_0 - \arctan x_0)} \lambda \quad (9)$$

where $x_0 = R_c/r_0$ and λ is the global mass-to-flux ratio for the core as a whole. For $x_0 = 3$, we have $\lambda_c = 3.21 \lambda$. In other words, the central part of their core is substantially less magnetized relative to mass than the core as a whole, due to the initial mass condensation.

For the $\lambda = 3$ case under consideration, we have $\lambda_c = 9.63$, which makes the material on the central flux tube rather weakly magnetized (relative to mass). The magnetization of the central region is important, because the central part is accreted first and the star formation efficiency in a core may not be 100% efficient (e.g., Alves et al. 2007). If we define as in §2 an effective mass-to-flux ratio for the (cylindrical) magnetic flux surface that encloses 1/3 of the core mass, then $\lambda_{\text{eff}} = 2.39\lambda$ for the density distribution adopted by JHC12 (equation [8]). It is significantly different from the effective mass-to-flux ratio of $\lambda_{\text{eff}} = 1.41\lambda$ for the uniform density that we adopted.

The above difference in λ_{eff} makes our strongest field case of $\lambda = 2.92$ ($\lambda_{\text{eff}} = 4.12$) more directly comparable to JHC12’s $\lambda = 2$ ($\lambda_{\text{eff}} = 4.78$) case. There is agreement that, in both cases, the formation of a RSD is suppressed, even when the tilt angle $\theta_0 = 90^\circ$. These results suggest that RSD formation is suppressed when the effective mass-to-flux ratio $\lambda_{\text{eff}} \lesssim 5$, independent of the degree of field-rotation misalignment, consistent with the conclusion we reached toward the end of §4 based on Models P and Q.

Similarly, JHC12’s $\lambda = 3$ ($\lambda_{\text{eff}} = 7.17$) models may be more directly comparable to our $\lambda = 4.86$ ($\lambda_{\text{eff}} = 6.85$) models. Our calculations show that a (more or less) rotationally supported disk is formed in the extreme $\theta_0 = 90^\circ$ case for $\lambda_{\text{eff}} = 6.85$ (Model H, see Fig. 7) but not in the intermediate tilt angle $\theta_0 = 45^\circ$ case (Model E). This is consistent with their Fig. 14, where a Keplerian disk is formed for $\theta_0 = 90^\circ$ for $\lambda_{\text{eff}} = 7.17$, but not for $\theta_0 = 45^\circ$. In the latter case, JHC12 found a disk-like structure with a flat rather than Keplerian rotation profile. They attributed the flat rotation to additional support from the magnetic energy, which dominates the kinetic energy at small radii. We believe that their high magnetic energy comes from strongly magnetized, low-density lobes (i.e., DEMS), which are clearly visible in our Model E (see Fig. 7). Although there is still significant rotation on the 10^2 AU scale in Model E, we find the morphology and kinematics of the circumstellar structure too disorganized to be called a “disk.” We conclude that for a moderate field strength corresponding to $\lambda_{\text{eff}} \sim 6\text{--}7$, a rotationally supported disk does not form except when the magnetic field is tilted nearly orthogonal to the rotation axis.

Our weak-field case of $\lambda = 9.72$ ($\lambda_{\text{eff}} = 13.7$) can be compared with JHC12’s $\lambda = 5$ ($\lambda_{\text{eff}} = 12.0$) case. In both cases, a well-defined rotationally supported disk is formed when $\theta_0 = 90^\circ$ (see our Fig. 7 and their Fig. 12). For the intermediate tilt angle $\theta_0 = 45^\circ$, JHC12 obtained a disk-like structure with a flat rotation curve, with the magnetic energy dominating the kinetic energy at small radii. This is broadly consistent with our intermediate tilt angle Model D, where a highly variable, “porous” disk is formed, with the central part often dominated by strongly magnetized, low-density lobes. There is also agreement that the disk formation is suppressed if $\theta_0 = 0$ even for such a weakly magnetized case. It therefore appears

that, for the weak-field case of $\lambda_{\text{eff}} \gtrsim 10$, a rotationally supported disk can be induced by a relatively moderate tilt angle of $\theta_0 \gtrsim 45^\circ$.

The result that a misalignment between the magnetic field and rotation axis helps disk formation by weakening magnetic braking may be counter-intuitive. Mouschovias & Paleologou (1979) showed analytically that, for a uniform rotating cylinder embedded in a uniform static external medium, magnetic braking is much more efficient in the orthogonal case than in the aligned case. This analytic result may not be directly applicable to a collapsing core, however. As emphasized by JHC12, the collapse drags the initially uniform, rotation-aligned magnetic field into a configuration that fans out radially. JHC12 estimated analytically that the collapse-induced field fan-out could in principle make the magnetic braking in the aligned case more efficient than in the orthogonal case. The analytical estimate did not, however, take into account of the angular momentum removal by outflow, which, as we have shown in §3.2, is a key difference between the weak-field ($\lambda = 9.72$, $\lambda_{\text{eff}} = 13.7$) aligned case (Model A) where disk formation is suppressed and its orthogonal counterpart (Model G) that does produce a rotationally supported disk (see Figs. 1 and 4, and also Ciardi & Hennebelle 2010).

The generation of a powerful outflow in the weak-field aligned case (Model A) is facilitated by the orientation of its pseudodisk, which is perpendicular to the rotation axis (see Fig. 2). This configuration is conducive to both the pseudodisk winding up the field lines and the wound-up field escaping above and below the pseudodisk, which drives a bipolar outflow. When the magnetic field is tilted by 90° away from the rotation axis, the pseudodisk is warped by rotation into a snail-shaped curtain that is unfavorable to outflow driving (see Fig. 2). The outflow makes it more difficult to form a rotationally supported disk in the aligned case. Disk formation is further hindered by magnetically dominated, low-density lobes (DEMS), which affect the inner part of the accretion flow of the aligned case more than that of the perpendicular case, at least when the field is relatively weak (see Fig. 1 and 7). For more strongly magnetized cases, the DEMS becomes more dynamically important close to the central object, independent of the tilt angle θ_0 (see Fig. 8). DEMS-like structures were also seen in some runs of JHC12 (e.g., the case of $\lambda = 2$ and $\theta_0 = 0^\circ$; see their Fig. 19) but were not commented upon. As stressed previously by Zhao et al. (2011) and Krasnopolsky et al. (2012) and confirmed by our calculations, the DEMS presents a formidable obstacle to the formation and survival of a rotationally supported disk.

5.2. Misalignment not Enough for Disk Formation in General

While there is agreement between JHC12 and our calculations that misalignment between the magnetic field and rotation axis is beneficial to disk formation, it is unlikely that

the misalignment alone can enable disk formation around the majority of young stellar objects. The reason is the following. Troland & Crutcher (2008) obtained a mean dimensionless mass-to-flux ratio of $\bar{\lambda}_{\text{eff}} \approx 2$ through OH Zeeman observations for a sample of dense cores in nearby dark clouds¹. For such a small λ_{eff} , disk formation is completely suppressed, even for the case of maximum misalignment of $\theta_0 = 90^\circ$. Crutcher et al. (2010) argued, however, that there is a flat distribution of the total field strength in dense cores, from $B_{\text{tot}} \approx 0$ to some maximum value $B_{\text{max}} \approx 30 \mu\text{G}$; the latter corresponds to $\lambda_{\text{eff}} \approx 1$, so that the mean $\bar{\lambda}_{\text{eff}}$ stays around 2. If this is the case, some cores could be much more weakly magnetized than others, and disks could form preferentially in these cores. However, to form a rotationally supported disk, the core material must have (1) an effective mass-to-flux ratio λ_{eff} greater than about 5 *and* (2) a rather large tilt angle (see discussion in the preceding section). If one assumes that the core-to-core variation of λ_{eff} comes mostly from the field strength rather than the column density (as done in Crutcher et al. 2010), then the probability of a core having $\lambda_{\text{eff}} \gtrsim 5$ (or $B_{\text{tot}} \lesssim 6 \mu\text{G}$) is $\sim 1/5$. Since a large tilt angle of $\theta_0 \sim 90^\circ$ is required to form a RSD for $\lambda_{\text{eff}} \sim 6\text{--}7$, the chance of disk formation is reduced from $\sim 1/5$ by at least a factor of 2 (assuming a random orientation of the magnetic field relative to the rotation axis), to $\sim 10\%$ or less.

The above estimate is necessarily rough, and can easily be off by a factor of two in either direction. It is, however, highly unlikely for the majority of the cores to simultaneously satisfy the conditions on both λ_{eff} and θ_0 for disk formation. The condition $\lambda_{\text{eff}} \gtrsim 5$ is especially difficult to satisfy because, as noted earlier, it implies that the dense cores probed by OH observations must have a total field strength $B_{\text{tot}} \lesssim 6 \mu\text{G}$, less than or comparable to the well-defined median field strength inferred by Heiles & Troland (2005) for the much more diffuse, cold neutral *atomic* medium (CNM). It is hard to imagine a reasonable scenario in which the majority of dense cores have magnetic fields weaker than the CNM.

We note that Krumholz et al. (2013) independently estimated a range of $\sim 10\text{--}50\%$ for the fraction of dense cores that would produce a Keplerian disk based on Fig. 14 of JHC12. Their lower limit of $\sim 10\%$ is in agreement with our estimate; in both cases, the fraction is dominated by weakly magnetized cores that have mass-to-flux ratios greater than 5 and moderately large tilt angles. Their upper limit of $\sim 50\%$ is much higher than our estimate, mainly because it includes rather strongly magnetized cores with mass-to-flux ratios as small as 2. Since our calculations show that such strongly magnetized cores do not

¹We assume that the mass-to-flux ratio measured by Troland & Crutcher on the core scale is the same as the effective mass-to-flux ratio near the core center because, for significantly magnetically supercritical cores, ambipolar diffusion is generally ineffective in reducing the value of λ near the center relative to that in the envelope.

produce rotationally supported disks even for large tilt angles, we believe that this upper limit may be overly generous.

Whether dense cores have large tilt angle θ_0 between the magnetic field and rotation axis that are conducive to disk formation is unclear. Hull et al. (2012) measured the field orientation on the 10^3 AU-scale for a sample of 16 sources using millimeter interferometer CARMA. They found that the field orientation is not tightly correlated with the outflow axis; indeed, the angle between the two is consistent with being random. If the outflow axis is aligned with the core rotation axis and if the field orientation is the same on the core scale as on the smaller, 10^3 AU-scale, then θ_0 would be randomly distributed between 0 and 90° , with half of the sources having $\theta_0 \geq 60^\circ$. However, the outflow axis may not be representative of the core rotation axis. This is because the (fast) outflow is thought to be driven magnetocentrifugally from the inner part of the circumstellar disk (on the AU-scale or less; Shu et al. 2000; Königl & Pudritz 2000). A parcel of core material would have lost most of its angular momentum on the way to the outflow launching location; the torque (most likely magnetic or gravitational) that removes the angular momentum may also change the direction of the rotation axis. Similarly, the field orientation on the 10^3 AU-scale may not be representative of the initial field orientation on the larger core scale. The magnetic field on the 10^3 AU scale is more prone to distortion by collapse and rotation than that on the core scale. Indeed, Chapman et al. (2013) found that the field orientation on the core scale measured using single-disk telescope CSO is within 20° of the outflow axis for 3 of the 4 sources in their sample; the larger angle measured in the remain source may be due projection effects because its outflow axis is close to the line-of-sight. If the result of Chapman et al. is valid in general and if the outflow axis reflects the core rotation axis, then dense cores with large tilt angle θ_0 would be rare. In this case, disk formation would be rare according to the calculations presented in this paper and in JHC12, even in the unlikely event that the majority of dense cores are as weakly magnetized as $\lambda_{\text{eff}} \gtrsim 5$.

Rotationally supported disks are observed, however, routinely around evolved Class II YSOs (see Williams & Cieza 2011 for a recent review), and increasingly around younger Class I (e.g., Jørgensen et al. 2009; Lee 2011; Takakuwa et al. 2012) and even Class 0 (Tobin et al. 2012) sources. When and how such disks form remain unclear. Our calculations indicated that the formation of large observable (10^2 AU-scale) rotationally supported disks² is difficult even in the presence of a large tilt angle θ_0 during the early protostellar accretion (Class 0)

²We cannot rule out the existence of small, AU-scale disks, because the size of our effective “sink particle” is 6.7 AU. Small disks may be needed to drive fast outflows during the Class 0 phase, and may form through non-ideal MHD effects (Machida et al. 2010; Dapp & Basu 2010; Dapp et al. 2012).

phase³. This may not contradict the available observations yet (Maury et al. 2010), since only one Keplerian disk is found around a (late) Class 0 source so far (L1527; Tobin et al. 2012); it could result from a rare combination of an unusually weak magnetic field and a large tilt angle θ_0 . If it turns out, through future observations using ALMA and JVLA, that large-scale Keplerian disks are prevalent around Class 0 sources, then some crucial ingredients must be missing from the current calculations. Possible candidates include non-ideal MHD effects and turbulence. The existing calculations indicate that realistic levels of the classical non-ideal MHD effects do not weaken the magnetic braking enough to enable large-scale disk formation (Mellon & Li 2009; Li et al. 2011; Krasnopolsky et al. 2012; see also Krasnopolsky & Königl 2002 and Braiding & Wardle 2012a,b), although misalignment has yet to be considered in such calculations. Supersonic turbulence was found to be conducive to disk formation (Santos-Lima et al. 2012, 2013; Seifried et al. 2012; Myers et al. 2012; Joos et al. 2013), although dense cores of low-mass star formation typically have subsonic non-thermal line-width and it is unclear whether subsonic turbulence can enable disk formation in dense cores magnetized to a realistic level. If, on the other hand, it turns out that large-scale Keplerian disks are rare among Class 0 sources, then the question of disk growth becomes paramount: how do the mostly undetectable Class 0 disks become detectable in the Class I and II phase? If the magnetic braking plays a role in keeping the early disk undetectable, then its weakening at later times may promote rapid disk growth. One possibility for the late weakening of magnetic braking is the depletion of the protostellar envelope, either by outflow stripping (Mellon & Li 2008) or accretion (Machida et al. 2011). It deserves to be better quantified.

5.3. Summary

We carried out a set of MHD simulations of star formation in dense cores magnetized to different degrees and with different tilt angles between the magnetic field and the rotation axis. We confirmed the qualitative result of Joos et al. (2012) that misalignment between the magnetic field and rotation axis tends to weaken magnetic braking and is thus conducive to disk formation. Quantitatively, we found however that the misalignment enables the formation of a rotationally supported disk only in dense cores where the star-forming material is rather weakly magnetized, with a dimensionless mass-to-flux ratio $\gtrsim 5$; large misalignment in such cores allows the rotation to wrap the equatorial pseudodisk in the aligned case into

³We are unable to follow the collapse until most of the core material is accreted into the central object for numerical reasons. Such a complete accretion may not be realistic, however, if the star formation efficiency in a core is typically as low as 1/3 (e.g., Alves et al. 2007).

a curved curtain that hinders outflow driving and angular momentum removal, making disk formation easier. In more strongly magnetized cores, disk formation is suppressed independent of the misalignment angle, because the inner part of the protostellar accretion flow is dominated by strongly magnetized, low-density regions. If dense cores are as strongly magnetized as inferred by Troland & Crutcher (2008; with a mean mass-to-flux ratio ~ 2), it would be difficult for the misalignment alone to enable disk formation in the majority of them. We conclude that how protostellar disks form remains an open question.

We thank Mark Krumholz for useful discussion. This work is supported in part by NASA grant NNX10AH30G and the Theoretical Institute for Advanced Research in Astrophysics (TIARA) in Taiwan through the CHARMS project.

REFERENCES

- Allen, A., Li, Z.-Y., & Shu, F. H. 2003, *ApJ*, 599, 363
- Alves, J., Lombardi, M., & Lada, C. J. 2007, *A&A*, 462, 17
- Bodenheimer, P. 1995, *ARA&A*, 33, 199
- Braiding, C. R., & Wardle, M. 2012, *MNRAS*, 422, 261
- Braiding, C. R., & Wardle, M. 2012, *MNRAS*, 427, 3188
- Burkert, A., & Bodenheimer, P. 2000, *ApJ*, 543, 822
- Chapman, N. et al. 2013, *ApJ*, submitted
- Ciardi, A., & Hennebelle, P. 2010, *MNRAS*, 409, L39
- Crutcher, R. M. 2012, *ARA&A*, 50, 29
- Crutcher, R. M., Wandelt, B., Heiles, C., Falgarone, E., & Troland, T. H. 2010, *ApJ*, 725, 466
- Dapp, W. B., & Basu, S. 2010, *A&A*, 521, 56
- Dapp, W. B., Basu, S., & Kunz, M. W. 2012, *A&A*, 541, A35
- Duffin, D. F. & Pudritz, R. E. 2009, *ApJ*, 706, L46
- Galli, D., Lizano, S., Shu, F. H., & Allen, A. 2006, *ApJ*, 647, 374

- Galli, D., & Shu, F. H. 1993, *ApJ*, 417, 243
- Goodman, A. A., Benson, P., Fuller, G. A., & Myers, P. C. 1993, *ApJ*, 406, 528
- Heiles, C., & Troland, T. H. 2005, *ApJ*, 624, 773
- Hennebelle, P., & Ciardi, A. 2009, *A&A*, 506, L29
- Hennebelle, P., & Fromang, S. 2008, *A&A*, 477, 9
- Hull, C. L. H. et al. 2012, arXiv1212.0540
- Joos, M., Hennebelle, P., & Ciardi, A. 2012, *A&A*, 543, A128
- Joos, M., Hennebelle, P., Ciardi, A., & Fromang, S. 2013, *A&A*, submitted, arXiv:1301.3004
- Jørgensen, J. K., van Dishoeck, E. F., Visser, R., Bourke, T. L., Wilner, D. J., Lommen, D., Hogerheijde, M. R., & Myers, P. C. 2009, *A&A*, 507, 861
- Königl, A. & Pudritz, R. 2000, in *Protostars and Planets IV*, eds. V. Mannings et al. (Univ. of Arizona Press), 759
- Krasnopolsky, R., & Königl, A. 2002, *ApJ*, 580, 987
- Krasnopolsky, R., Li, Z.-Y., & Shang, H. 2010, *ApJ*, 716, 1541
- Krasnopolsky, R., Li, Z.-Y., & Shang, H. 2011, *ApJ*, 733, 54
- Krasnopolsky, R., Li, Z.-Y., Shang, H., & Zhao, B. 2012, *ApJ*, 757, 77
- Krumholz, M. R., Crutcher, R. M., & Hull, C. L. H. 2013, *ApJ*, submitted
- Lee, C. F. 2011, *ApJ*, 741, 62
- Li, Z.-Y., Krasnopolsky, R., & Shang, H. 2011, *ApJ*, 738, 180
- Machida, M. N., Inutsuka, S., & Matsumoto, T. 2010, arXiv:1009.2140
- Machida, M. N., Inutsuka, S., & Matsumoto, T. 2011, *PASJ*, 63, 555
- Machida, M. N., Matsumoto, T., Hanawa, T., & Tomisaka, K. 2006, *ApJ*, 645, 1227
- Matsumoto, T., & Tomisaka, K. 2004, *ApJ*, 616, 266
- Maury, A. J., André, P., Hennebelle, P., Motte, F., Stamatellos, D., Bate, M., Belloche, A., Duchêne, G., & Whitworth, A. 2010, *A&A*, 512, A40

- Myers, A. T., McKee, C. F., Cunningham, A. J., Klein, R. I., & Krumholz, M. R. 2012, arXiv:1211.3467 (submitted to ApJ)
- Mellon, R. R., & Li, Z.-Y. 2008, ApJ, 681, 1356
- Mellon, R. R., & Li, Z.-Y. 2009, ApJ, 698, 922
- Mouschovias, T. Ch., & Paleologou, E. V. 1979, ApJ, 230, 204
- Price, D. J., & Bate, M. R. 2007, Ap&SS, 311, 75
- Santos-Lima, R., de Gouveia Dal Pino, E. M., & Lazarian, A. 2012, ApJ, 747, 21
- Santos-Lima, R., de Gouveia Dal Pino, E. M., & Lazarian, A. 2013, MNRAS, in press
- Seifried, D., Banerjee, R., Klessen, R. S., Duffin, D., & Pudritz, R. E. 2011, MNRAS, 417, 1054
- Seifried, D., Banerjee, R., Pudritz R., & Klessen, R. S. 2012, MNRAS, 423, 40
- Shu, F. H., Najita, J. R., Shang, H., & Li, Z.-Y. 2000, in Protostars and Planets IV, eds. V. Mannings et al. (Univ. of Arizona Press), 789
- Takakuwa, S, Saito, M., Lim, J., Saigo, K., Sridharan, T. K., & Patel, N. A. 2012, ApJ, 754, 52
- Tobin, J. J., Hartmann, L., Chiang, H.-F., Wilner, D. J., Looney, L. W., Loinard, L., Calvet, N., & D’Alessio, P. 2012, Nature, 492, 83
- Tomida, K., Tomisaka, K., Matsumoto, T., Hori, Y., Okuzumi, S., Machida, M. N., & Saigo, K. 2013, ApJ, 763, 6
- Tomisaka, K. 1998, ApJ, 502, L163
- Troland, T. H., & Crutcher, R. M. 2008, ApJ, 680, 457
- Williams, J. P., & Cieza, L. A. 2011, ARA&A, 49, 67
- Zhao, B., & Li, Z.-Y. 2013, ApJ, 763, 7
- Zhao, B., Li, Z.-Y., Nakamura, F., Krasnopolsky, R., & Shang, H. 2011, ApJ, 742, 10

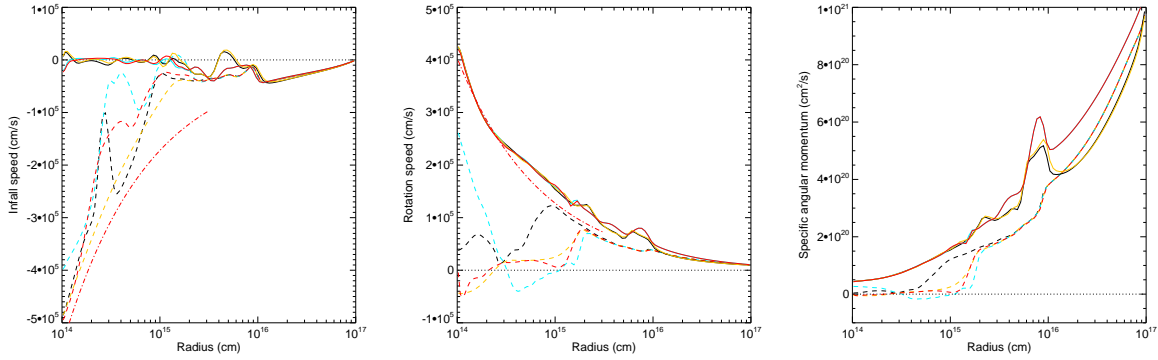


Fig. 5.— Infall (left panel) and rotation (middle) speed and the specific angular momentum (right) on the equatorial plane along 4 representative directions for the aligned (dashed lines) and orthogonal (solid) case. For comparison, the free-fall speed for the aligned case and the Keplerian profile for the orthogonal case are plotted as dotted-dash line in the left and middle panel respectively. It is evident that a rotationally supported disk is formed in the orthogonal but not the aligned case. In the latter case, the specific angular momentum of the equatorial flow decreases significantly upon entering the pseudodisk at $\sim 10^{16}$ cm and the DEMS-dominated region around $\sim 10^{15}$ cm.

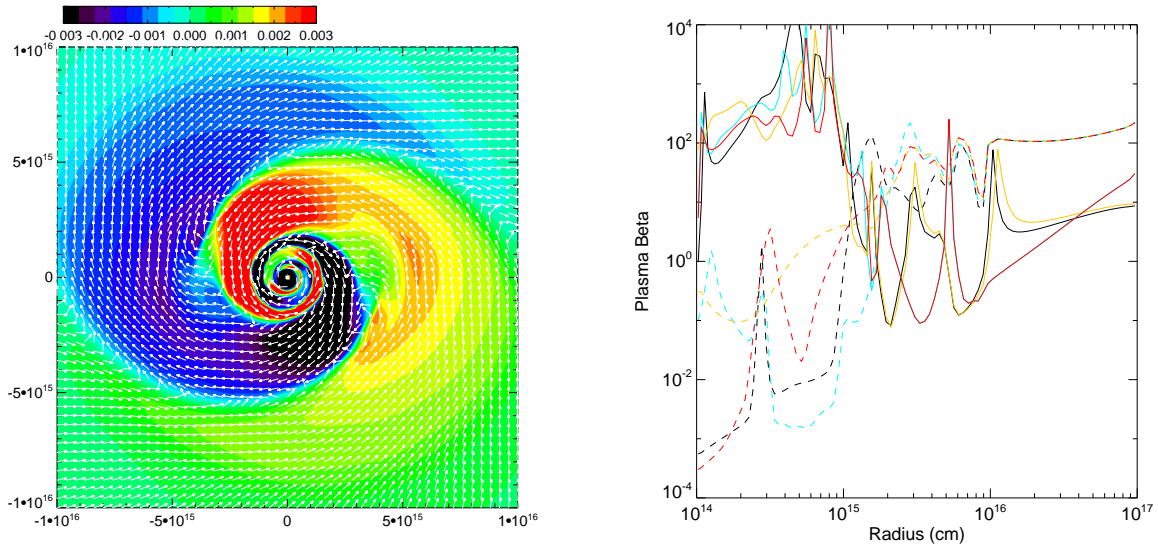


Fig. 6.— Left: Same as Fig. 3, except that the color map is for the toroidal component of the equatorial magnetic field (rather than density), showing the inward spiraling of two strains of magnetic field lines of opposite polarity. For clarity, the plotted field strength is capped from above and below at $\pm 3 \times 10^{-3}$ G. Right: The plasma β along 4 representative directions in the equatorial plane showing that the inner 100 AU region in the orthogonal case (i.e., on the Keplerian disk; solid lines) is dominated by thermal rather than magnetic pressure, whereas the opposite is true for the aligned case (dashed).

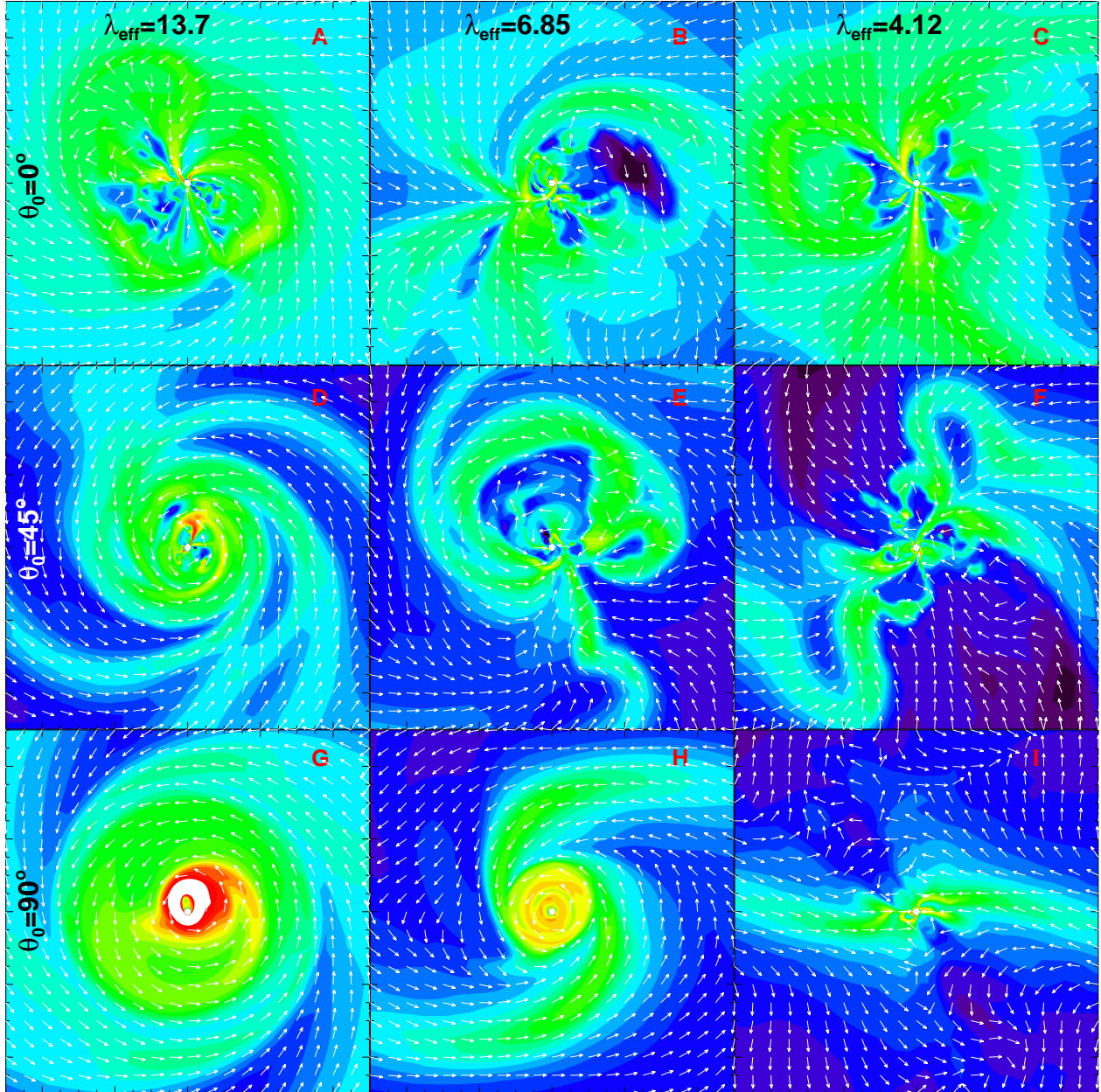


Fig. 7.— Snapshots of Models A–I (see Table 1 for model parameters) when the central mass reaches $0.2 M_{\odot}$. Plotted are maps of the logarithm of density (color range: -18 to -12) and velocity unit vectors on the equatorial plane. The box size in each panel is 10^{16} cm.

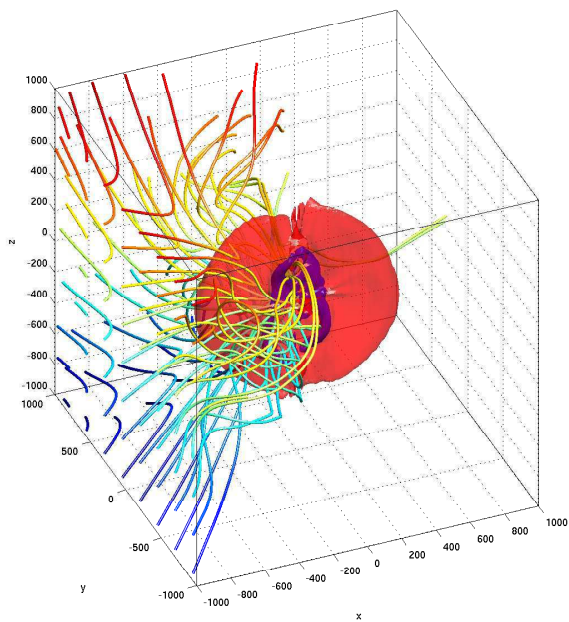
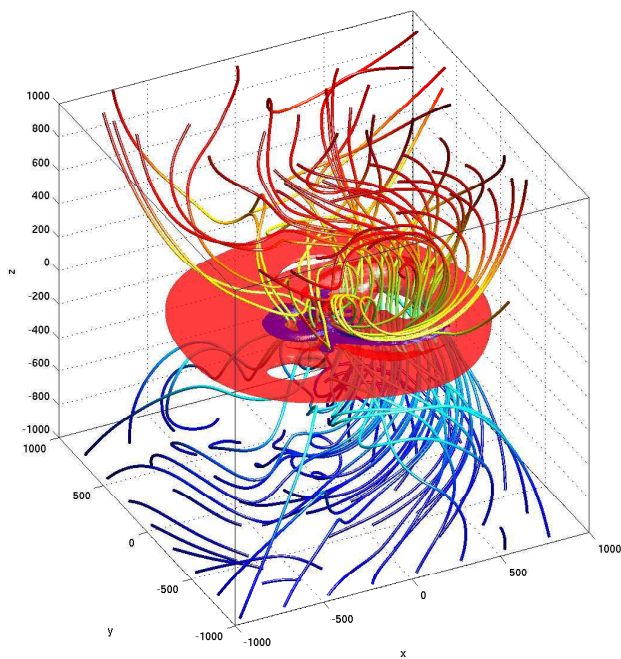


Fig. 8.— Same as in Fig. 2, but for the stronger field ($\lambda = 2.92$) cases of Model C (aligned) and Model I (orthogonal) at a time when the central mass reaches $0.2 M_{\odot}$. For clarity, only field lines originated from the bottom x - y and left y - z plane are plotted, respectively. Note the difference in orientation of the pseudodisks in the two cases. The inner part of both pseudodisks is dominated by low-density, strongly magnetized regions. The length is in units of AU.